

# NONLINEAR RECEPTIVITY TO OBLIQUE VORTICAL MODES IN FLOW PAST AN ELLIPTIC LEADING EDGE

Lars-Uve Schrader<sup>1</sup>, Catherine Mavriplis<sup>2</sup>

Department of Mechanical Engineering  
University of Ottawa, ON, Canada K1N 6N5

<sup>1</sup>lschrade@uOttawa.ca, <sup>2</sup>Catherine.Mavriplis@uOttawa.ca

Luca Brandt<sup>3</sup>, Dan S. Henningson<sup>4</sup>

Linné Flow Centre, KTH Mechanics  
Royal Institute of Technology (KTH), 100 44 Stockholm, Sweden

<sup>3</sup>luca@mech.kth.se, <sup>4</sup>henning@mech.kth.se

## ABSTRACT

Boundary layer receptivity to pairs of unsteady oblique freestream vortical modes is studied in direct numerical simulation of flow over a flat plate with an elliptic leading edge. The freestream is perturbed by three types of oblique Fourier modes, differing in the magnitude of the three vorticity components. The vortical modes excite steady boundary layer streaks, and the associated receptivity mechanism is nonlinear in the forcing amplitude. Leading edges with two different aspect ratios are considered. It is found that the streak amplitudes obtained are largely unaffected by the leading edge bluntness. Whereas linear receptivity is the predominant mechanism at low forcing frequencies, the nonlinear mechanism becomes important when high-frequency vortices are present in the freestream. Nonlinear receptivity is therefore expected to contribute significantly to the excitation of boundary layer streaks by freestream turbulence.

## INTRODUCTION

Receptivity is the initial stage of laminar-turbulent transition in boundary layers. The term denotes the mechanism by which freestream fluctuations or corrugations of an aerodynamic surface are converted into boundary layer instabilities. Here, we present a direct numerical simulation (DNS) study of receptivity to oblique freestream vortical modes in boundary layer flow over a flat plate with an elliptic leading edge.

Oblique-mode transition is a simple model for bypass transition due to freestream turbulence. Berlin *et al.* (1994) study by DNS the laminar-turbulent transition of a Blasius boundary layer under the action of pairs of oblique vortical freestream modes. Three steps are identified: the nonlinear generation of streamwise vortices by the oblique modes, the formation of boundary layer streaks due to these vortices and the secondary streak instability. The work by Berlin & Henningson (1999) focuses on the receptivity phase, where single freestream vortical modes and pairs of oblique waves act as triggers of instability. The Blasius boundary layer is

found to be particularly receptive to single modes with significant streamwise vorticity. The receptivity mechanism is linear in the forcing amplitude and produces streamwise elongated boundary layer streaks. Similar streaks are forced by the oblique modes via a nonlinear receptivity mechanism. A weakly nonlinear perturbation model by Brandt *et al.* (2002) is able to reproduce the streak generation by oblique modes.

The study of nonlinear effects on the streak formation in boundary layers is motivated by the observation that linear theories underpredict the streak amplitudes typically found in experiments with freestream turbulence. Leib *et al.* (1999) state that “nonlinear effects play an important role in the development of Klebanoff modes in many of the most important experiments”. The authors conjecture that “this [nonlinear] effect increases with increasing downstream distance from the leading edge and possibly with increasing frequency” and that “the nonlinear effects may enter in a more or less quasi-steady manner”. These statements motivate the present work, where the nonlinear boundary layer response to freestream vortical modes with different frequencies is studied. The leading edge is included and its shape is varied to identify bluntness effects on the nonlinear receptivity. This paper follows a similar study of linear receptivity to vortical modes on the same geometry (Schrader *et al.*, 2010).

## FLOW CONFIGURATION

We study flow over a flat plate with leading edge (Figure 1a), where the leading edge is shaped as a modified superellipse (Figure 1b). Lin *et al.* (1992) are the first considering this contour, because it features smoothness in wall curvature and hence a reduction of receptivity at the junction. We denote the streamwise, vertical and spanwise directions by  $x$ ,  $y$  and  $z$  and the respective velocities by  $U$ ,  $V$  and  $W$  (baseflow) and  $u$ ,  $v$  and  $w$  (disturbance). All lengths are scaled by the short semi-axis  $b$  of the leading edge. The long semi-axis  $a = AR \cdot b$  determines the bluntness of the nose, where  $AR$  stands for the aspect ratio of the leading edge. Here, we consider  $AR = 6$

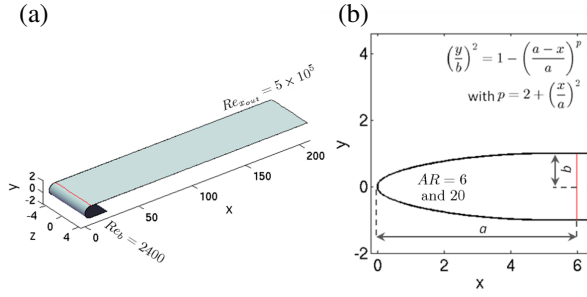


Figure 1. (a) Flat plate with elliptic leading edge ( $AR = 6$ ). Lengths are normalized by half-thickness  $b$  of plate. Red line: leading edge junction. (b) Modified super-ellipse (MSE), representing leading edge shape.

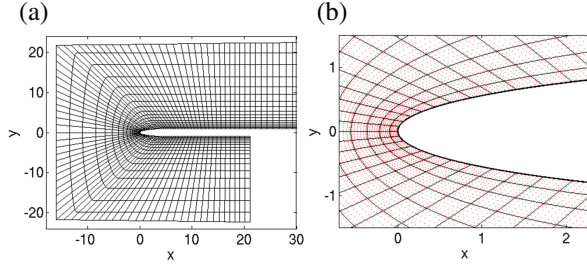


Figure 2. Spectral element mesh ( $AR = 6$  leading edge). (a) Inflow region, (b) close-up view of leading edge. Spectral elements (black boxes) and GLL nodes (red dots).

and 20. These values are also used in earlier numerical studies (e.g. Lin *et al.*, 1992; Wanderley & Corke, 2001; Schrader *et al.*, 2010). The reference speed is the freestream velocity  $U_\infty$  and the flow conditions are defined by the Reynolds number  $Re = U_\infty b / \nu = 2400$ . The outflow boundary is located at  $x_{out} = 208.34b$  so that the outflow Reynolds number is  $Re_{out} = U_\infty x_{out} / \nu = 5 \times 10^5$ .

## NUMERICAL METHOD

The simulations are carried out using the three-dimensional incompressible Navier-Stokes solver *Nek5000* (Fischer *et al.*, 2008) based on the spectral element method (SEM). The SEM combines the high accuracy of global spectral methods with the geometrical flexibility of finite element methods and is suitable for high fidelity simulations of flow around bodies with surface curvature and leading edges. The physical domain is decomposed into spectral elements, upon which the solution is approximated by tensor products of Legendre polynomial Lagrangian interpolants. In one dimension, the Legendre expansion is written as

$$q^{(l)}(r) = \sum_{n=0}^N q_n^{(l)} L_n(r), \quad (1)$$

where  $q$  is a flow variable (e.g. streamwise velocity),  $r$  is the local spatial coordinate of element  $l$ ,  $L_n$  is the  $n^{th}$  order Legendre polynomial,  $q_n$  is the spectral coefficient and  $N$  is the

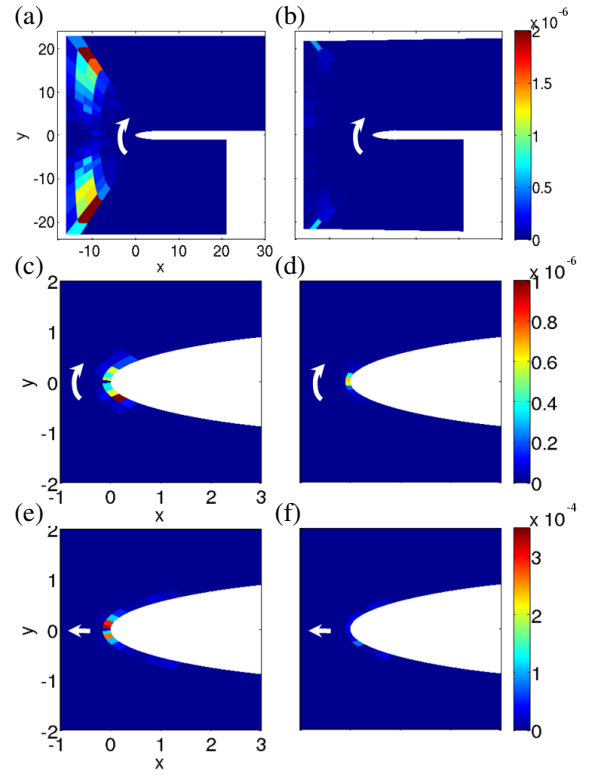


Figure 3. Error estimators of streamwise mean flow on initial SEM mesh (from Schrader *et al.*, 2010, a,c,e) and improved mesh (b,d,f). Leading edge with  $AR = 6$ . White arrows indicate local elemental direction along which error estimators were computed.

highest polynomial degree included. The spatial allocation of the integration nodes is based on Gauss-Lobatto-Legendre (GLL) and Gauss-Legendre (GL) quadratures for the velocity and pressure fields, respectively. Here, we choose  $N = 7$  for the velocity grid and  $N = 5$  for the pressure grid, following the  $\mathbb{P}_N - \mathbb{P}_{N-2}$  discretization of Maday & Patera (1989). This results in a staggered pressure grid with regard to the velocity grid, obviating the possibility of spurious pressure modes and rendering pressure boundary conditions unnecessary.

The computational mesh (Figure 2) is similar to the grids used by Schrader *et al.* (2010); however, the freestream boundary is streamline-shaped instead of straight. This is advantageous when freestream disturbances are convected downstream. For the three-dimensional simulations, 7650 elements are used, which amounts to nearly 2.8 million degrees of freedom. Dirichlet conditions for the mean velocity at the inflow and the freestream boundaries are generated from a potential flow solution including the streamline displacement by the boundary layer (see Schrader *et al.*, 2010). No-slip, no-stress and periodic conditions are applied at the wall, the outflow and the lateral boundaries, respectively.

## Error Estimator

The quality of the flow solution on a given computational mesh can be assessed by computing *a posteriori* error estimators. This is carried out here for two-dimensional simulations

of the streamwise mean flow around the leading edge with  $AR = 6$ . The error estimator (Mavriplis, 1990) is defined as

$$\varepsilon = \sqrt{\frac{q_N^2}{\frac{1}{2}(2N+1)} + \int_{N+1}^{\infty} \frac{q_n^2}{\frac{1}{2}(2n+1)} dn}. \quad (2)$$

The quantity  $q_N$  is the highest-order spectral coefficient of (1), while the coefficients  $q_n$  for order  $N+1$  and higher are estimated by an extrapolation of the spectrum (of the streamwise mean velocity here), using the exponential-decay relation  $q_n = ce^{-\sigma n}$ . The constant  $c$  and the decay rate  $\sigma$  are obtained through a least squares best fit of the last four points ( $N-3, \dots, N$ ) of the resolved spectrum to an exponential decay.

The error estimator was originally developed to devise criteria for spectral-element mesh adaptation (Mavriplis, 1994). Here, we use  $\varepsilon$  to investigate the error of the streamwise mean velocity on a given mesh and improve the mesh manually as indicated by  $\varepsilon$ . Because  $\varepsilon$  estimates the one-dimensional spectrum of the elemental approximation, we obtain  $N+1$  values of  $\varepsilon$  for each local direction per element. Averaging  $\varepsilon$  over these  $N+1$  values yields two error estimators per element for a two-dimensional simulation (one in each direction). The initial mesh (from Schrader *et al.*, 2010) produces an uneven error distribution in the inflow region (Figure 3a) and relatively large errors at the leading edge (Figures 3c,e), where the white arrows indicate the elemental direction of the error evaluation. This information is used to derive an improved numerical mesh (Figures 3b,d,f), where we only redistribute the elements while leaving the total number of elements and the spectral order unchanged. The major benefit of the improved mesh is an increase of time step size and an ensuing reduction of simulation time by approximately 10%.

### Freestream Disturbance

Pairs of oblique vortical modes serve as a simple model of freestream turbulence. The vortical disturbances are prescribed as Fourier modes with spatial and temporal periodicity, where streamwise periodicity is replaced by time periodicity invoking Taylor's hypothesis. The modal amplitude functions are those of Schrader *et al.* (2010), where three different types are used, labeled as  $\xi$ -,  $\eta$ - and  $\zeta$ -modes. This denotation indicates the dominant component of the vorticity vector  $(\xi, \eta, \zeta)$  of these modes. Schrader *et al.* (2010) point out that only two linearly independent vortical modes exist, the  $\xi$ - and the  $\zeta$ -modes (labeled B and A modes in Bertolotti, 1997), whereas the third type (the  $\eta$ -mode) is not a physically independent solution. It is nonetheless convenient to introduce all three modes because vortical modes with only one single vorticity component can easily be derived from the  $\xi$ -,  $\eta$ - and  $\zeta$ -modes. This is extensively utilized by Schrader *et al.* (2010) in a study of linear receptivity to purely streamwise, vertical and spanwise freestream vorticity.

The inflow wave vector is  $(\gamma, \beta) = (0.48, \pm 0.72)$ , with  $\gamma$  and  $\beta$  being the vertical and spanwise wavenumbers. These values are consistent with those in Schrader *et al.* (2010); the only difference is that we also include the mode with spanwise wavenumber  $\beta = -0.72$  and add it to the mode with

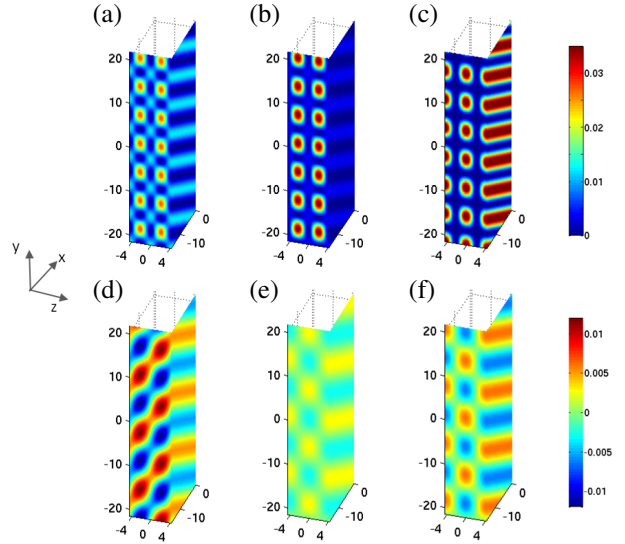


Figure 4. Inflow disturbance of pairs of oblique vortical modes (frequency  $F = 96$ , wave vector  $(\gamma, \beta) = (0.48, \pm 0.72)$ , amplitude  $\varepsilon_v = 3.54 \times 10^{-3}$ ). Velocity magnitude of (a)  $\xi$ -modes, (b)  $\eta$ -modes, (c)  $\zeta$ -modes. Streamwise vorticity of (d)  $\xi$ -modes, (e)  $\eta$ -modes, (f)  $\zeta$ -modes.

$\beta = +0.72$ . This produces a freestream vortical disturbance consisting of two oblique waves. The disturbance is scaled to obtain an amplitude of  $\varepsilon_v = \sqrt{\mathbf{u}_{in}^2}/2$ , where  $\mathbf{u}_{in}$  is the disturbance-velocity vector at the computational inflow,

$$\mathbf{u}_{in} = \Re\{\hat{\mathbf{u}} e^{i(\gamma y \pm \beta z - \omega t)}\}, \quad (3)$$

with  $\Re$  denoting the real part. The quantity  $\hat{\mathbf{u}}$  is the modal velocity coefficient and depends on the mode type ( $\xi$ -,  $\eta$ - or  $\zeta$ -mode; see Schrader *et al.*, 2010, for details). The angular frequency  $\omega$  is replaced by the frequency parameter  $F = [\omega/(U_\infty^2/\nu)] \times 10^6$  here. Figure 4 shows the velocity magnitude and streamwise vorticity of inflow disturbances made up of pairs of oblique  $\xi$ -,  $\eta$ - and  $\zeta$ -modes (frequency  $F = 96$ , wave vector  $(\gamma, \beta) = (0.48, \pm 0.72)$ , amplitude  $\varepsilon_v = 3.54 \times 10^{-3}$ ). The  $\xi$ -modes feature the largest and the  $\eta$ -modes the smallest streamwise vorticity.

## RESULTS

The boundary layer response to a pair of oblique  $\xi$ -modes with frequency  $F = 96$  manifests itself mainly in the streamwise velocity (Figure 5a). The upstream disturbance features the short streamwise length scale of the freestream modes (enforced by the frequency), whereas the dominant downstream structure is streamwise elongated. Not only the streamwise scale but also the spanwise wavelength change in downstream direction (doubling of the spanwise wavenumber, Figure 5b). We summarize that the receptivity mechanism to high-frequency oblique freestream modes consists of two steps: the linear excitation of fundamental disturbances followed by a nonlinear self-interaction of the fundamental mode. Streamwise elongated streaks with twice the spanwise

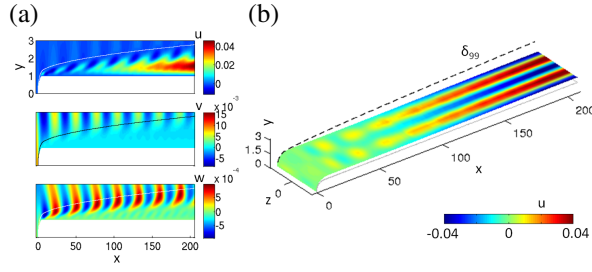


Figure 5. boundary layer response to pair of oblique  $\xi$ -modes ( $F = 96$ ,  $(\gamma, \beta) = (0.48, \pm 0.72)$ ,  $\varepsilon_v = 3.54 \times 10^{-3}$ ). (a)  $x$ - $y$  plane of streamwise, vertical and spanwise disturbance velocities ( $z = 2.05$ ). Thin lines:  $\delta_{99}$ . (b) Horizontal plane of streamwise disturbance at  $y(\max_y(u_{rms}))$ .

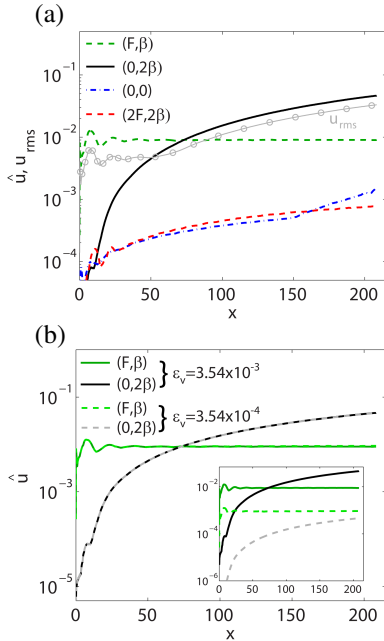


Figure 6. (a) Temporal-spanwise Fourier decomposition of boundary layer disturbance excited by pair of oblique  $\xi$ -modes ( $F = 96$ ,  $(\gamma, \beta) = (0.48, \pm 0.72)$ ,  $\varepsilon_v = 3.54 \times 10^{-3}$ ). (b) Comparison of fundamental mode  $(F, \beta)$  and spanwise super-harmonic  $(0, 2\beta)$  for two forcing amplitudes:  $\varepsilon_v = 3.54 \times 10^{-3}$  and  $3.54 \times 10^{-4}$ .

wavenumber of the freestream modes arise from this process. These streaks attain significantly larger amplitudes than the upstream fundamental disturbance.

A temporal-spanwise Fourier decomposition of the total boundary layer disturbance ( $u_{rms}$  curve in Figure 6a) confirms that the upstream disturbance is dominated by a fundamental short-scale mode, whereas the downstream disturbance evolution is mainly attributable to steady streaks with twice the fundamental spanwise wavenumber. The steadiness of these streaks becomes manifest as an elongation of the disturbance structure (zero streamwise wavenumber, cf. Figure 5b). This confirms that nonlinear effects appear “in a more or less quasi-steady manner” (Leib *et al.*, 1999, cf. Introduction). The

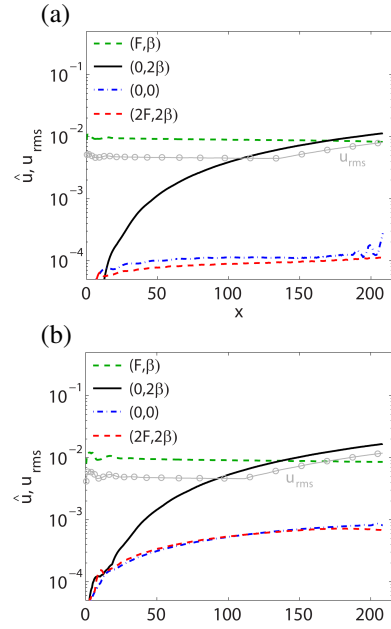


Figure 7. Temporal-spanwise Fourier decomposition of boundary layer disturbance excited by pair of oblique (a)  $\eta$ -modes and (b)  $\zeta$ -modes ( $F = 96$ ,  $(\gamma, \beta) = (0.48, \pm 0.72)$ ,  $\varepsilon_v = 3.54 \times 10^{-3}$ ).

third and fourth most important contributions to the boundary layer disturbance are the mean-flow modification  $(0, 0)$  and the double-frequency mode  $(2, \pm 2)$  (Figure 6a).

The nature of the boundary layer receptivity is clarified by matching the evolution curves obtained for two different forcing amplitudes  $\varepsilon_v$ . The unsteady fundamental mode amplitude is found to be linear in  $\varepsilon_v$ , whereas the steady streak amplitude scales as  $\varepsilon_v^2$  (Figure 6b). The strong steady streak disturbance is hence generated by quadratic self-interaction of the unsteady fundamental mode. The amplitudes of the modes  $(0, 0)$  and  $(2, \pm 2)$  are also proportional to  $\varepsilon_v^2$  (not shown). Linear and nonlinear receptivity processes thus act simultaneously in boundary layers exposed to high-frequency freestream fluctuations. The nonlinear receptivity process obeys the two-step mechanism explained by Brandt *et al.* (2002), where the generation of streamwise vortices by the oblique modes precedes the excitation of boundary layer streaks by these vortices (lift-up mechanism).

When exposed to oblique  $\eta$ - and  $\zeta$ -modes, the boundary layer develops steady disturbance streaks, too, but these streaks have lower amplitudes than those forced by the  $\xi$ -modes (Figure 7). Because the  $\xi$ -modes feature a larger streamwise vorticity component than the  $\eta$ - and  $\zeta$ -modes (Figure 4), we conclude that the boundary layer is nonlinearly most receptive to streamwise vorticity, as in the case of linear receptivity (Schrader *et al.*, 2010). Interestingly, the  $(0, 0)$  and  $(2, \pm 2)$  components amplify less in an environment of oblique  $\eta$ -modes than in the presence of the other two mode types (Figure 7a).

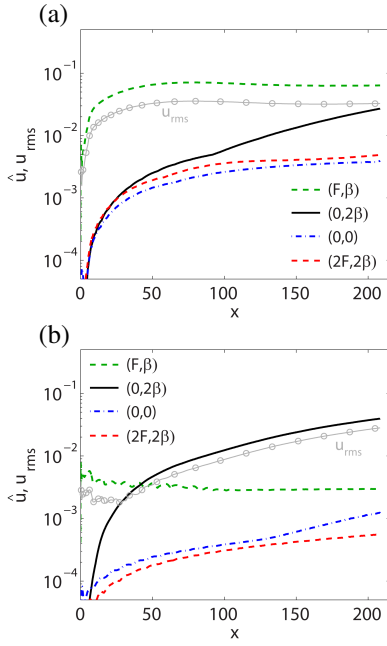


Figure 8. Temporal-spanwise Fourier decomposition of boundary layer disturbance excited by pair of oblique  $\xi$ -modes  $((\gamma, \beta) = (0.48, \pm 0.72))$ ,  $\epsilon_v = 3.54 \times 10^{-3}$ . Forcing frequency (a)  $F = 16$ , (b)  $F = 192$ .

### Frequency Effects

Leib *et al.* (1999) conjecture that nonlinear effects on the streak development may be more relevant at high frequencies. This is confirmed here by comparing the standard case ( $F = 96$ ) with two cases at a lower and a higher forcing frequency ( $F = 16$  and  $F = 192$ ), using oblique freestream waves of the  $\xi$ -type. For  $F = 16$ , the disturbance ( $u_{rms}$ -curve) is made up mostly of the fundamental unsteady mode, whereas the steady double-spanwise wavenumber streak hardly contributes to  $u_{rms}$  (Figure 8a). The dominant receptivity mechanism of  $\xi$ -modes with  $F = 16$  is thus linear (cf. Schrader *et al.*, 2010). In contrast, the boundary layer destabilization by oblique  $\xi$ -modes with  $F = 192$  is almost entirely due to nonlinear receptivity, resulting in steady streaks (Figure 8b).

### Bluntness Effects

So far, only the leading edge with aspect ratio  $AR = 6$  has been used. In order to study leading edge bluntness effects, we now also consider a more slender leading edge ( $AR = 20$ ) and compare six different simulations (two leading edges times three mode types,  $\xi$ ,  $\eta$  and  $\zeta$ , at frequency  $F = 96$ ). It is found that the flow response to all three types of freestream vorticity is largely unaffected by the leading edge shape (Figure 9a). We further confirm that the boundary layer is nonlinearly most receptive to oblique  $\xi$ -modes and least receptive to  $\eta$ -modes.

Schrader *et al.* (2010) demonstrate that linear boundary layer receptivity to purely vertical freestream vorticity is particularly efficient in flows with blunt leading edges. Key to the mechanism is the generation of streamwise vorticity due to stretching and tilting of the vertical vorticity at the leading edge. Schrader *et al.* (2010) construct the purely vertical

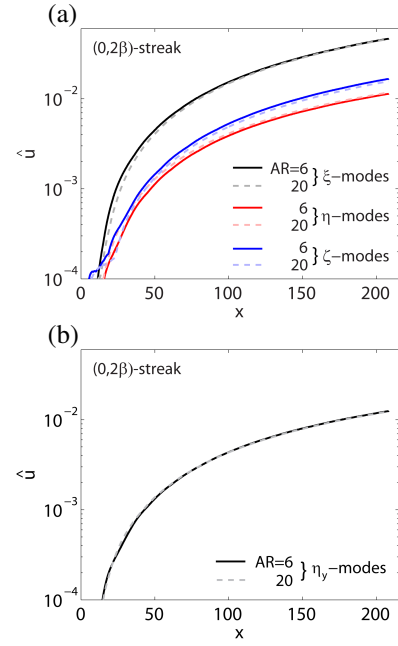


Figure 9. Nonlinear receptivity to pairs of oblique modes. Comparison for two leading edges ( $AR = 6$  and  $20$ ).  $(0, 2\beta)$ -streak amplitude due to (a)  $\xi$ -,  $\eta$ - and  $\zeta$ -modes ( $F = 96$ ,  $(\gamma, \beta) = (0.48, \pm 0.72)$ ,  $\epsilon_v = 3.54 \times 10^{-3}$ ) and (b)  $\eta_y$ -modes ( $\gamma = 0$ ,  $F = 96$ ,  $\beta = \pm 0.72$ ,  $\epsilon_v = 3.54 \times 10^{-3}$ ).

vorticity modes (denoted ‘ $\eta_y$ -modes’) by setting the vertical wavenumber  $\gamma$  of the  $\eta$ -modes to zero. Here, we use pairs of oblique  $\eta_y$ -modes at frequency  $F = 96$ , invoking the nonlinear receptivity mechanism, and vary the leading edge shape. Again, a change of bluntness does not alter the streak amplitude (Figure 9b). It is concluded that the bluntness-dependent vortex stretching and tilting mechanisms do not play any significant role in nonlinear receptivity. Instead, the streamwise vorticity required for effective streak excitation is mainly generated by the nonlinear interaction between the oblique freestream modes. This mechanism is shown here to be independent of the leading edge shape.

### Nonlinear versus Linear Receptivity

Here, we compare the downstream evolution of two steady boundary layer streaks ( $F = 0$ ) with the same spanwise wavenumber ( $\beta = 1.44$ ), but different origin: the first streak is excited by a pair of oblique  $\xi$ -modes with frequency  $F = 96$  (nonlinear receptivity), whereas the second streak is triggered by a single  $\xi$ -mode with frequency  $F = 0$  (linear receptivity). The two streaks amplify at different streamwise rates (Figure 10), because they are generated in different regions of the boundary layer. The linear receptivity mechanism is initiated right at the leading edge, where it produces significant upstream transient growth. The nonlinear process, a two-step mechanism, acts over a longer extent of the boundary layer so that the nonlinear streak fully emerges farther downstream (in different flow conditions). Matching the streak amplitudes at a certain downstream location ( $Re_x = 2 \times 10^5$  in Figure 10) enables us to assess the relative importance of linear and non-

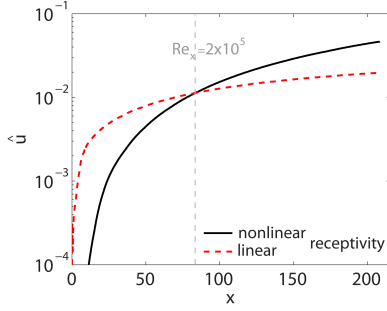


Figure 10. Streamwise development of two steady streaks ( $\beta = 1.44$ ) triggered via nonlinear and linear receptivity. Streak due to linear receptivity is scaled to match amplitude at  $Re_x = 2 \times 10^5$  of streak due to nonlinear receptivity.

linear receptivity. To this end, we write the streak amplitude  $A_{str}$  as

$$\begin{aligned} A_{str} &= C_{lin} \varepsilon_{v,lin} \\ A_{str} &= C_{nln} \varepsilon_{v,nln}^2 \end{aligned} \quad (4)$$

where  $\varepsilon_{v,lin}$  and  $\varepsilon_{v,nln}$  are the forcing amplitudes of the linear and nonlinear receptivity mechanisms, and  $C_{lin}$  and  $C_{nln}$  are the local ( $Re_x$ -dependent) linear and nonlinear receptivity coefficients. For the example of  $Re_x = 2 \times 10^5$ , we read off from Figure 10 a streak amplitude of  $A_{str} = 0.0113$ . With  $\varepsilon_{v,lin} = 2.92 \times 10^{-4}$  and  $\varepsilon_{v,nln} = 3.54 \times 10^{-3}$ , we obtain  $C_{lin} = 38.73$  and  $C_{nln} = 904.45$ . Equating the two relations in (4) identifies an amplitude threshold  $\varepsilon_{thresh} = C_{lin}/C_{nln}$ , above which the nonlinearly excited streak becomes stronger at a certain streamwise location ( $Re_x$ ) than the streak due to linear receptivity. For  $Re_x = 10^5$  ( $2 \times 10^5; 5 \times 10^5$ ), we find  $\varepsilon_{thresh} = 0.093$  (0.043; 0.018). These thresholds are large, suggesting that linear receptivity is more effective than nonlinear receptivity. Because the downstream growth rate of the nonlinear streak exceeds that of the linear streak, the relative importance of nonlinear receptivity is enhanced with increasing Reynolds number. Moreover,  $\varepsilon_{thresh}$  depends on the frequency of the oblique vortical modes triggering the nonlinear streak.

## CONCLUSIONS

Leib *et al.* (1999) notice a discrepancy between Klebanoff-mode amplitudes observed in experiments and streak amplitudes obtained from linear receptivity and instability theories. Therefore, nonlinear (quadratic) boundary layer receptivity to unsteady freestream vorticity is studied here. To this end, we perform DNS of flow past an elliptic leading edge, considering pairs of oblique vortical freestream modes. The spectral element method used proves to be particularly efficient when combined with an error-estimator based mesh improvement.

When exposed to oblique vortical modes, the boundary layer develops steady, energetic disturbance streaks, provided that the frequency of the modes is high enough. The largest streak amplitudes are obtained when the freestream

modes bear mainly streamwise vorticity. The streak intensity is largely unaffected by the leading edge shape, irrespective of the type of freestream disturbance (dominant vorticity component). This is in contrast to linear receptivity, where blunt leading edges enhance the receptivity to vertical freestream vorticity (Schrader *et al.*, 2010), and suggests that nonlinear receptivity studies in Blasius flow are still valid in flows with leading edges. Although linear receptivity is more effective, nonlinear receptivity is expected to be significant in flows with freestream turbulence because of the energy concentration in the higher-frequency range of the turbulent spectrum.

The authors gratefully acknowledge funding by VR (The Swedish Research Council) and NSERC (Natural Sciences and Engineering Research Council of Canada), and computer time by SNIC/NSC (National Supercomputer Centre, Linköping universitet).

## REFERENCES

- Berlin, S. & Henningson, D. 1999 A nonlinear mechanism for receptivity of free-stream disturbances. *Phys. Fluids* **11** (12), 3749–3760.
- Berlin, S., Lundbladh, A. & Henningson, D. 1994 Spatial simulations of oblique transition in a boundary layer. *Phys. Fluids* **6** (6), 1949–1951.
- Bertolotti, F. P. 1997 Response of the Blasius boundary layer to free-stream vorticity. *Phys. Fluids* **9** (8), 2286–2299.
- Brandt, L., Henningson, D. S. & Ponziani, D. 2002 Weakly non-linear analysis of boundary layer receptivity to free-stream disturbances. *Phys. Fluids* **14**, 1426–1441.
- Fischer, P., Kruse, J., Mullen, J., Tufo, H., Lottes, J. & Kerkemeier, S. 2008 *NEK5000 - Open Source Spectral Element CFD solver*. <https://nek5000.mcs.anl.gov/index.php/MainPage>.
- Leib, S. J., Wundrow, D. W. & Goldstein, M. E. 1999 Effect of free-stream turbulence and other vortical disturbances on a laminar boundary layer. *J. Fluid Mech.* **380**, 169–203.
- Lin, N., Reed, H. & Saric, W. 1992 Effect of leading edge geometry on boundary-layer receptivity to freestream sound. In *Instability, Transition and Turbulence* (ed. M. Hussaini, A. Kumar & C. Streett). Springer.
- Maday, Y. & Patera, A. T. 1989 Spectral element methods for the Navier-Stokes equations. In *State of the Art Surveys in Computational Mechanics* (ed. A. K. Noor), pp. 71–143. ASME, New York.
- Mavriplis, C. 1990 A posteriori error estimators for adaptive spectral element techniques. In *Notes on Numerical Fluid Mechanics* 29 (ed. P. Wesseling), pp. 333–342. Braunschweig: Vieweg.
- Mavriplis, C. 1994 Adaptive mesh strategies for the spectral element method. *Comput. Methods Appl. Mech. Engrg.* **116**, 77–86.
- Schrader, L.-U., Brandt, L., Mavriplis, C. & Henningson, D. S. 2010 Receptivity to free-stream vorticity of flow past a flat plate with elliptic leading edge. *J. Fluid Mech.* **653**, 245–271.
- Wanderley, J. B. V. & Corke, T. C. 2001 Boundary layer receptivity to free-stream sound on elliptic leading edges of flat plates. *J. Fluid Mech.* **429**, 1–21.